

# Defect-free and defective adaptations of crystalline sheets to stretching deformation

Ranzhi Sun and Zhenwei Yao\*

*School of Physics and Astronomy, and Institute of Natural Sciences,  
Shanghai Jiao Tong University, Shanghai 200240, China*

The elastic response of the crystalline sheet to the stretching deformation in the form of wrinkles has been extensively investigated. In this work, we extend this fundamental scientific question to the plastic regime by exploring the adaptations of crystalline sheets to the large uniaxial mechanical stretching. We reveal the intermittent plastic shear deformations leading to the complete fracture of the sheets wrapping the cylinder. Specifically, systematic investigations of crystalline sheets of varying geometry show that the fracture processes can be classified into defect-free and defective categories depending on the emergence of topological defects. We highlight the characteristic mechanical and geometric patterns in response to the large stretching deformation, including the shear-driven intermittent lattice tilting, the vortex structure in the displacement field, and the emergence of mobile and anchored dislocations as plastic excitations. The effects of noise and initial lattice orientation on the plastic deformation of the stretched crystalline sheet are also discussed. These results advance our understanding of the atomic level on the irreversible plastic instabilities of 2D crystals under large uniaxial stretching and may have potential practical implications in the precise engineering of structural instabilities in packings of covalently bonded particulate systems.

## I. INTRODUCTION

Stretching a free-standing thin elastic sheet leads to the nonintuitive wrinkling behavior for relaxing the in-plane strain incompatibility generated by the Poisson effect [1–3]. The wrinkles are parallel to the direction of the applied tension in both rectangular [1, 4] and annular elastic sheets [5, 6], and they provide a means for mechanical characterization of stretchable soft solid membranes that have practical implications [7–10]. The wrinkle structure arising in various stretched elastic systems has been extensively studied by experimental [6, 11, 12], computational [13–15], and theoretical [1, 4, 5, 16, 17] approaches. While the elastic response of the elastic sheet to the stretching deformation in the form of wrinkles has been systematically investigated, irreversible plastic instabilities of an intact crystalline sheet, which are inevitable in the large stretching regime of real systems [11, 18, 19], have not yet been fully explored especially on the microscopic level. Understanding the plasticity of an intact crystalline sheet fabricated by regular packings of particles in triangular lattice under large stretching deformation is of fundamental and practical significance. Especially, it has a strong connection to the important subject of mechanical instabilities involved in a host of physical processes, including the failure of 2D crystalline materials [20–25], crystal growth on interfaces [26–29], and 2D assemblies of colloids [30–32] and viral shells [33–35].

The goal of this work is to explore how the crystalline sheet consisting of Lennard-Jones (L-J) particles in triangular lattice adapts to the large uniaxial mechanical stretching, focusing on the characteristic mechanical and geometric structures arising from the irreversible plastic instabilities. In our model, to avoid any complication

caused by the boundary condition, the stretching deformation is imposed on the crystalline sheet by wrapping it around the cylindrical substrate that is subject to controllable gradual expansion; the cylindrical surface provides the geometric constraint only and no friction is involved. The formally simple L-J potential is employed to study the plastic deformation process for its featured energy minimum structure, and it has also been extensively used to model various chemical and physical bonds in condensed matter systems [36, 37]. This model contains the essential elements for us to study plastic instabilities of mechanically stressed regular packings of particles that can be modeled as an isotropic elastic sheet in the continuum limit [3, 38]. Note that the model of the crystalline sheet wrapping on the cylinder is also connected to the cylindrical crystal, which arises in many contexts, including the cylindrical packings of disks and spheres, phyllotaxis (“leaf arrangement”) in botany, colloids on the surface of a liquid film coating a solid cylinder, and cell walls of rod-shaped bacteria such as *E. coli* [39–44].

The main results of this work are presented below. We first perform preliminary theoretical analysis on the homogeneous elastic deformation of the crystalline sheet under small stretching and confirm the reliability of the computational approach. In the regime of large stretching, we reveal the intermittent nature of the plastic shear deformations leading to the complete fracture (disconnection) of the crystalline sheet wrapping the cylinder. The fracture processes are classified into defect-free and defective categories depending on the emergence of topological defects. In defect-free plastic shear deformations, we observe the tilting of the entire lattice, which is quantitatively analyzed by a geometric model. We also highlight the vortex structure formed in the shear-driven displacement field and the associated glide motion of dislocations. Defective plastic deformations tend to occur in wider crystalline sheets, where the emergent topological defects are anchored in space serving as the seeds

---

\*zyao@sjtu.edu.cn

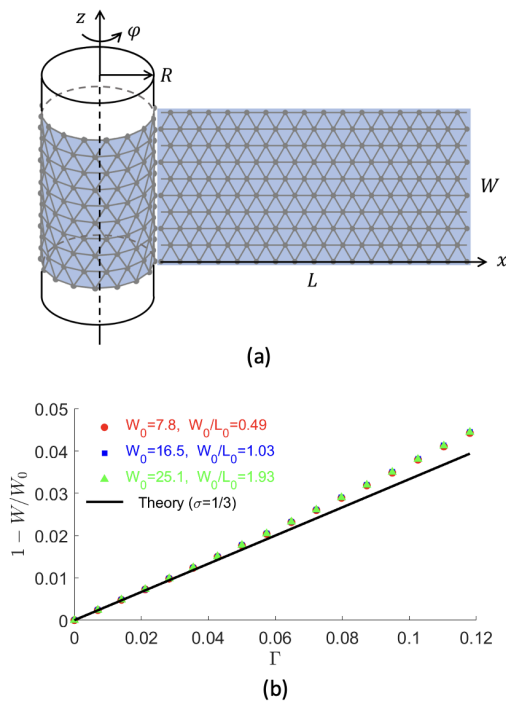


FIG. 1: The schematic plot of the model system and the preliminary theoretical analysis. (a) The model system consists of a crystalline elastic sheet wrapping a cylinder under gradual expansion. The expanded crystalline sheet is also shown in the  $x$ - $z$  plane. (b) Plots of  $1 - W/W_0$  against the expansion factor  $\Gamma$  in the elastic deformation regime for the crystalline sheet of typical geometries.  $W$  and  $W_0$  are the width of the crystalline sheet before and after the deformation. The simulation data could be well fitted by the theoretical lines based on the linear elasticity theory up to  $\Gamma = 0.04$ .

for subsequent fracture events. The fracture processes of crystalline sheets of varying geometry are characterized by the sequences of defining plastic events; the results are summarized in the phase diagram. The effects of noise and initial lattice orientation on the plastic deformation of the stretched crystalline sheet are also discussed. These results advance our understanding of the atomic level on the plastic instabilities of 2D crystals under large uniaxial stretching and may have potential practical implications in the precise engineering of structural instabilities in packings of covalently bonded particulate systems.

## II. MODEL AND METHOD

The model system consists of the crystalline sheet wrapping a cylinder, as shown in Fig. 1(a). The crystalline sheet is fabricated by the L-J particles in triangular lattice. The cylindrical substrate provides the geometric constraint; there is no friction between the crystalline sheet and the cylinder. The upper and lower edges of the crystalline sheet are free of external stress. No

external constraints other than the contact with the frictionless cylindrical surface are imposed to the crystalline sheet. The particle interact by the Lennard-Jones potential:

$$V(r_{ij}) = 4\epsilon_0 \left[ \left( \frac{\sigma_0}{r_{ij}} \right)^{12} - \left( \frac{\sigma_0}{r_{ij}} \right)^6 \right], \quad (1)$$

where  $r_{ij}$  is the distance of particles  $i$  and  $j$  in three-dimensional space. The L-J potential curve reaches the minimum value  $V_{min} = -\epsilon_0$  at the balance distance of  $r_0 = 2^{1/6}\sigma_0$ .

In the initial state, the stress-free crystalline sheet of length  $L_0$  and width  $W_0$  wraps on the cylinder of radius  $R_0$ .  $L_0 = 2\pi R_0$ . The cylinder is subject to controllable gradual expansion at a given rate. Specifically, the radius of the cylinder is enlarged by a factor of  $1 + p$  in each expansion. In simulations, the parameter  $p$  is sufficiently small ( $p = 0.7\%$ ) to fulfill the quasi-static condition. The particle configuration is subsequently relaxed to the lowest energy state after each expansion, which is realized by the standard steepest descent method in simulation [45]. The step size  $s = 5 \times 10^{-4}$ . In the relaxation of the stretched crystalline sheet on the expanded cylinder of a given radius, the energy of the system is reduced deep to the energy valley typically after  $10^5$  updates of the particle configuration. After the  $n$ -th expansion, the radius of the cylinder becomes  $R_n = (1 + p)R_{n-1}$ . The total expansion factor after  $n$  expansions is

$$\Gamma_n = \frac{R_n - R_0}{R_0} \quad (2)$$

The resulting particle configurations in mechanical equilibrium are analyzed from both geometric and topological perspectives, including the variations of the tilt angle and bond length, and the topological transformations of the lattice via the Delaunay triangulation in the plastic deformations of the stretched crystalline sheet [46]. In this work, the units of length and energy are chosen to be the parameters  $r_0$  and  $\epsilon_0$  associated with the L-J potential, respectively. No cut-off length of the L-J potential is introduced in simulations.

## III. RESULTS AND DISCUSSION

This section consists of four subsections. In Sec. III A, we perform preliminary theoretical analysis on the homogeneous deformation of the crystalline sheet under small stretching. In Sec. III B, we discuss the defect-free intermittent plastic shear deformations upon large stretching. Specifically, we analyze the lattice tilting phenomenon and establish its connection to plastic shear deformations quantitatively based on a geometric model. We also analyze the variation of bond length, the displacement field, and the associated glide motion of dislocations in plastic shear deformations. In Sec. III C, we discuss a distinct fracture mechanism based on the proliferation of topological defects. The defective plastic deformations tend

to occur in wider crystalline sheets, where the emergent topological defects are anchored in space serving as the seeds for subsequent fracture events. The fracture processes of crystalline sheets of varying geometry are characterized by the sequences of defining plastic events. The results are summarized in the phase diagram. In Sec. III D, we discuss the effects of noise and initial lattice orientation on the plastic deformation of the stretched crystalline sheet.

#### A. Homogeneous elastic deformation under small expansion

The crystalline sheet consisting of L-J particles in triangular lattice, which is confined on the cylindrical geometry, is initially stress free. With the gradual expansion of the cylinder, the in-plane stress accumulates over the lattice. Here, we first resort to the continuum elasticity theory to analyze the small deformation of the crystalline lattice on the early stage of the expansion process. By comparing with the numerical results, we also check the reliability of the computational approach, which shall be used to explore the interested regime of large deformation.

The triangular lattice is modeled as a two-dimensional continuous and isotropic elastic sheet [38]. Due to its zero Gaussian curvature, the cylindrical surface could be isometrically mapped to the plane [47]. This allows us to solve for the in-plane strain field in the Cartesian coordinates  $\{x, z\}$ , as shown in Fig. 1(a).  $x = R\varphi$ , where  $\varphi$  is the polar angle in the cylindrical coordinates. Here, for convenience, the vertical axis in the Cartesian coordinates is also denoted as  $z$ .

Now, we derive for the strain field over the stretched crystalline sheet in mechanical equilibrium from the force balance equation  $\partial_i \sigma_{ij} = 0$ , where  $i, j = x, z$ , and by the following stress-strain relation for the longitudinal deformation of the elastic membrane on the  $x$ - $z$  plane [38]

$$\begin{aligned}\sigma_{xx} &= \frac{E}{1 - \sigma^2}(u_{xx} + \sigma u_{zz}), \\ \sigma_{zz} &= \frac{E}{1 - \sigma^2}(u_{zz} + \sigma u_{xx}), \\ \sigma_{xz} &= \frac{E}{1 + \sigma}u_{xz},\end{aligned}\quad (3)$$

where  $\sigma$  is the Poisson's ratio, and  $E$  is the Young's modulus. As a boundary condition,  $\sigma_{zz} = 0$  on the upper and lower boundaries of the rectangular crystalline sheet. The sheet is horizontally stretched by a factor of  $\Gamma$ . We thus obtain the expressions for the strain field:

$$\begin{aligned}u_{xx} &= \Gamma \\ u_{zz} &= -\sigma u_{xx} = -\sigma\Gamma \\ u_{xz} &= u_{zx} = 0.\end{aligned}\quad (4)$$

According to Eqs.(4), the strain field established in the gently stretched crystalline sheet in mechanical equilibrium is homogeneous. Furthermore, a circumferential

stretch by the factor of  $\Gamma$  leads to a transverse compression by the factor of  $\sigma\Gamma$ . Note that  $\sigma = 1/3$  for the 2D isotropic elastic medium composed of L-J particles in triangular lattice [24, 48, 49]. From Eqs.(4), we obtain the only non-zero component of the stress tensor:

$$\sigma_{xx} = E\Gamma, \quad (5)$$

which is independent of the Poisson's ratio.

To check the reliability of the computational approach, we examine the variation of the width of the crystalline sheet in the expansion of the cylinder in simulations, and compare the numerical and theoretical results. We first present the analytical expression for the width of the crystalline sheet at the expansion factor  $\Gamma$  according to the second equation in Eqs.(4):

$$1 - \frac{W}{W_0} = \sigma\Gamma. \quad (6)$$

In Fig. 1(b), we present the plots of  $1 - W/W_0$  against the expansion factor  $\Gamma$ . It turns out that the simulation data for the crystalline sheets of varying width  $W_0$  and aspect ratio  $W_0/L_0$  collapse on the same series of dots. It indicates that the relation of  $1 - W/W_0$  and  $\Gamma$  is independent of the geometry of the crystalline sheet. The agreement of the simulation data and the theoretical result in Fig. 1(b) shows the reliability of the computational approach and the validity of the linear elasticity theory in describing the elastic deformation of the L-J crystalline sheet at least up to  $\Gamma = 0.04$ .

#### B. Defect-free intermittent plastic shear deformations

##### 1. Shear-driven lattice tilting

To explore the response of the crystalline sheet upon the gradual expansion of the cylinder, we first analyze a typical example case presented in Fig. 2. An important observation is the tilting of the strongly stretched crystalline lattice. The tilting phenomenon is quantified in the plot of the tilt angle  $\theta$  against the expansion factor  $\Gamma$  in Fig. 2(a).  $\theta$  is the angle between the tilted lattice and the  $x$  axis in the expanded planar crystalline sheet over the  $x$ - $z$  plane. In the quasi-static expansion process, the tilt angles of the bonds (with respect to  $\vec{e}_\varphi$ ) in the mechanically relaxed crystalline lattice at each value of  $\Gamma$  are recorded. The mean value and the standard deviation are plotted by the black curves with error bars. The mean value of the tilt angle reflects the tilting of the entire crystalline lattice.

A salient feature of the  $\theta$ -curve is that the variation of the tilt angle  $\theta$  exhibits the step-like behavior. With the expansion of the cylinder, the value of  $\theta$  is increased intermittently at a series of critical values of  $\Gamma$ , which are denoted as  $\Gamma_1, \Gamma_2 \dots \Gamma_f$  in Fig. 2(a). At  $\Gamma = \Gamma_f$ , the crystalline sheet is completely fractured, meaning that the sheet wrapping the cylinder becomes disconnected.

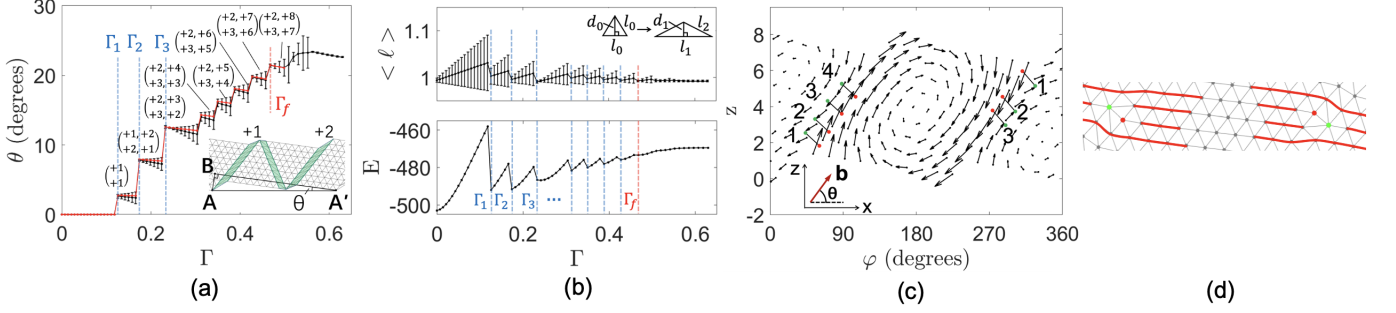


FIG. 2: The adaptation of the crystalline sheet to the gradual expansion of the cylinder leads to the intermittent plastic shear deformations. The particle configurations in mechanical equilibrium in the stretching process are analyzed from the perspectives of the tilt angle (a), the bond length and energy (b), and the displacement vector field (c).  $\Gamma = 0.22$  in (c). (d) Illustration of the pair of dislocations at the shear bands. The red and green dots represent five- and seven-fold disclinations.  $L_0 = 16.0$  and  $W_0 = 7.8$ .

As a practical criterion, the crystalline sheet wrapping the cylinder is regarded as being completely fractured when the width of the narrowest neck of two detaching lattice patches is less than about two lattice spacings. On the early stage of the expansion process ( $\Gamma < \Gamma_1$ ), the crystalline lattice is subject to homogeneous deformation, and the tilt angle remains zero until  $\Gamma$  reaches the first critical value  $\Gamma_1$ ;  $\Gamma_1 \approx 0.12$  for the case in Fig. 2(a). Between two consecutive critical values of  $\Gamma$ , it is noticed that the tilt angle is slightly declined. It suggests that the lattice tends to tilt back to fit the expanding cylinder. The tilt-back mode is energetically favored in comparison with the pure stretching mode, which can be qualitatively understood by considering a tilted straight 1D lattice with respect to the horizontal reference line. By tilting back towards the reference line (even without stretching the 1D lattice), the projected length of the 1D lattice along the reference line is increased.

We examine the particle configurations in mechanical equilibrium in the expansion process and find that the crystalline lattice experiences mechanical instability in the form of irreversible plastic shear deformation at each critical values of  $\Gamma$ . A typical plastically sheared particle configuration is shown in the inset of Fig. 2(a). The shear bands resulting from the plastic deformation are highlighted in green. These observations suggest that the entire plastic deformation process of the crystalline sheet could be characterized by the series of symbols  $\Gamma_i$ , each of which represents a plastic event in the expansion of the crystalline sheet.

In the following, we shall show that the orientation of the shear band is determined by the maximization of the shear stress as well as the orientation of the crystalline lattice. Over the expanded crystalline sheet on the  $x$ - $z$  plane as shown in Fig. 1(a), the uniaxial stretching along the  $x$  axis induces the non-zero component of the stress tensor  $\sigma_{xx}$  in Eq.(5);  $\sigma_{zz} = 0$  due to the stress-free boundary condition. To derive for the direction along which the shear stress reaches maximum, we rotate the Cartesian coordinates  $(x, z)$  counterclockwise by angle

$\alpha$  and work in the rotated Cartesian coordinates  $(x', z')$ . For simplicity, the components of the vector  $\vec{r}$  are denoted as  $(x_1 = x, x_2 = z)$  and  $(x'_1 = x', x'_2 = z')$  in the original and rotated coordinates, respectively. These components are related by the following relation:

$$x'_i = A_{ij}x_j. \quad (7)$$

$A_{ij}$  is the component of the rotation matrix  $\mathbf{A}$ :

$$\mathbf{A} = \begin{pmatrix} \cos \alpha & \sin \alpha \\ -\sin \alpha & \cos \alpha \end{pmatrix} \quad (8)$$

The components of the stress tensor in the rotated Cartesian coordinates are:

$$\sigma'_{ij} = A_{il}A_{jm}\sigma_{lm}, \quad (9)$$

in which the orthogonality condition of the rotation matrix is used;  $\mathbf{A}^{-1} = \mathbf{A}^T$ .

We finally obtain the shear stress in the  $(x', z')$  coordinates as:  $\sigma'_{12} = -\frac{1}{2}E\Gamma \sin(2\alpha)$ , whose magnitude reaches maximum at  $\alpha = \pi/4$  (and  $\alpha = 3\pi/4$ ). Therefore, the crystalline sheet is subject to maximum shear stress along the oblique line that makes the angle  $\pi/4$  with respect to the  $x$  axis. In other words, the  $\pi/4$  angle represents the direction along which the applied uniaxial stretching is most effectively converted into shear stress. Here, we shall point out that the orientation of maximum shear stress originates from the transformation of the applied uniaxial stress tensor, and it is independent of the microscopic interaction among the constituents composing the isotropic elastic medium. However, simulations show that the microscopic crystalline structure further restricts the orientation of the shear band. In the plastic shear deformation of the crystalline lattice at the tilt angle of  $\pi/3$ , as shown in Fig. 2(a), the shear band is along the inclined principal axis of the crystalline lattice whose angle with respect to the  $x$  axis ( $\pi/3$ ) is closest to the theoretically predicted value of  $\pi/4$  based on the continuum model. Fig. 2(a) shows that subsequent successive fracture of the crystalline lattice is along the formed shear bands, leading to the intermittent increase of the

tilt angle  $\theta$ . Furthermore, considering that the plastic shear deformation involves the enlarged separation of adjacent particles, the formation of the shear band structure may be inhibited if the particle-particle attraction increases with distance, which is opposite to the L-J potential. To test this point, we perform simulations with harmonic potential in the cases of  $L_0 = (10, 20, 30)$  and  $W_0 = (10, 20, 30)$ ; the crystalline sheet consists of a triangular lattice of linear springs. It turns out that under the harmonic potential, no shear band appears in the stretched crystalline lattice (at least up to  $\Gamma = 0.5$ ).

In the inset of Fig. 2(a), we see that steps are formed symmetrically on the upper and lower boundaries of the lattice as a consequence of the plastic shear deformation. The emergent step structure changes the morphology of the lattice boundary and breaks the originally  $C_k$  symmetry of the system, where  $k$  is the number of particles on the crystalline line along the circumferential direction. The lattice tilting could be attributed to these steps, which will be discussed later. Here, the steps-caused undulation of the lattice boundary is distinct from the undulation phenomenon driven by the Asaro-Tiller-Grinfeld (ATG) instability [28, 50–52]. In the latter case, the wave-like undulation developed on the stressed boundary of the 2D or 3D elastic medium results from the instability for initial perturbations of short wavelength, and mass transport is involved in the ATG instability. In the pure mechanical system of the crystalline sheet wrapping the cylinder, the stepped undulation of the boundary spontaneously occurs in the absence of any initial perturbation and surface diffusion.

Now, we characterize the observed step structure on the boundaries of the stretched crystalline sheet. The state of the plastically sheared crystalline lattice could be described by a series of numbers, each of which indicates the height and direction of a step. For example, the numbers above the particle configuration in the inset of Fig. 2(a) indicate the height of the two steps on the upper boundary (in the unit of lattice spacing). The positive sign is to indicate an upward step (in the top view of the system in the counterclockwise direction). In Fig. 2(a), the two arrays of numbers in the bracket indicate the heights of the steps located on the upper and lower boundaries, respectively. The dynamics of the steps is constructed by tracking the variation of these numbers. Specifically, on the  $\theta$ -curve in Fig. 2(a), we see that as the value of  $\Gamma$  exceeds  $\Gamma_3$ , the numbers in both columns increase by one, indicating that the height of the two pairs of steps on both sides of the lattice simultaneously increases by one lattice spacing. At the following larger critical values of  $\Gamma$ , the numbers on the right column increase by one or two each time, and those on the left column are invariant. It indicates that a pair of steps rise by one or two lattice spacings each time, and the height of the other pair of steps remains invariant in the expansion process.

Geometric analysis shows that the formation of the step structure on the boundaries of the crystalline sheet

caused by the plastic shear deformations is the key to the observed lattice tilting. In the following, we shall show that the total number of steps determines the tilt angle, regardless of the specific distribution of the steps on the boundaries.

Our calculations are based on the typical plastically sheared lattice in the inset of Fig. 2(a). To measure the tilt angle, we first connect the two identical points  $A$  and  $A'$  by a horizontal line on the plane of the unfolded cylindrical surface. Along the lattice line, we draw the line  $A'B$  and make the right triangle  $\triangle ABA'$ . All of the steps on the lower boundary of the lattice are enclosed in the triangle  $\triangle ABA'$ . The tilt angle  $\theta$  is the angle between the lines  $A'A$  and  $A'B$ . Based on this geometric model, geometric arguments show that

$$\sin \theta = \frac{\sqrt{3}}{4\pi} \frac{\ell(\Gamma)}{R(\Gamma)} N_s, \quad (10)$$

where  $N_s$  is the total number of steps enclosed in the triangle  $\triangle ABA'$ ,  $\ell$  is the bond length, and  $R$  is the radius of the cylinder. Simulations show that the relative variations of the bond length in the stretched lattices are small in comparison with the mean bond length even in the strongly stretched regime. As such, it is assumed that the bond length takes a uniform value  $\ell(\Gamma)$  in Eq.(10). Equation(10) shows that  $\sin \theta$  is proportional to the total number of steps  $N_s$ , and its dependence on the expansion factor  $\Gamma$  is through the quantities  $\ell(\Gamma)$  and  $R(\Gamma)$ .

According to Eq.(10), the tilt angle  $\theta$  versus the expansion factor  $\Gamma$  is plotted by the red curves in Fig. 2(a). To obtain the  $\theta$ -curve, at each value of  $\Gamma$ , we calculate the mean bond length of the stretched lattice in mechanical equilibrium for the value of the quantity  $\ell(\Gamma)$ , and count the total number of steps  $N_s$ . Figure 2(a) shows that the numerical results (the black curve with error bars) are well fitted by the red curve based on the geometric model in Eq.(10). The small deviation of the black and red curves between consecutive critical values of  $\Gamma$  can be attributed to the overestimated value of  $\ell(\Gamma)$  in Eq.(10). Specifically, the mean bond length that is used in the plot of the theoretical curve is slightly larger than the actual length of the bonds along the direction of the line  $AB$  in the inset of Fig. 2(a) due to the Poisson effect. Overall, the agreement of the numerical and theoretical results shows the validity of the geometric model for quantitatively understanding the tilting phenomenon caused by the plastic shear deformations.

In preceding paragraphs, we show that the crystalline sheet adapts to the expanding cylindrical substrate via the stretching and the tilting modes for the case in Fig. 2. Specifically, prior to the occurrence of the first plastic shear deformation, the response of the lattice is to stretch the bond length in the circumferential direction and simultaneously squeeze the lattice in the perpendicular direction; the tilt angle remains invariant. The adjustment of the bond length conforms to the mechanical laws of continuum elasticity theory. Once the expansion factor  $\Gamma$  reaches a series of critical values, the adaptation of

the crystalline sheet to the expanding cylinder is through the tilting of the entire lattice, which is realized by the plastic shear deformations. The connection of the tilting phenomenon and the plastic shear deformations of the strongly stretched crystalline lattice is established based on the geometric model.

## 2. Geometric analysis of bond length and displacement field

We proceed to analyze the variation of the bond length in the plastic shear deformation of the case in Fig. 2(a). In the upper panel in Fig. 2(b), the mean bond length  $\langle \ell \rangle$  is plotted against the expansion factor  $\Gamma$ . The standard deviation of the bond length distribution is indicated by the error bars. Note that the bonds on the boundary are excluded in the statistical analysis of the bond length.

From the upper panel in Fig. 2(b), we see that the  $\langle \ell \rangle$ - $\Gamma$  curve exhibits the zig-zag behavior. In the expansion process up to  $\Gamma \approx 0.5$ , the  $\langle \ell \rangle$ - $\Gamma$  curve conforms to the following pattern: the value of the mean bond length increases linearly with the expansion factor  $\Gamma$  and then rapidly falls down. In this process, the magnitude of the variation of  $\langle \ell \rangle$  is reduced with the increase of  $\Gamma$ . Scrutiny of the particle configurations in mechanical equilibrium indicates that each turning point of the  $\langle \ell \rangle$ - $\Gamma$  curve exactly corresponds to the plastic shear deformations of the lattice. The series of the critical values of  $\Gamma$  in Fig. 2(b) are identical to those in Fig. 2(a), where the plastic shearing events are analyzed in terms of the tilt angle. Examination of the variation of the energy reveals the abrupt decline of the energy at these critical values of  $\Gamma$ , as shown in the lower panel of Fig. 2(b).

From the  $\langle \ell \rangle$ - $\Gamma$  curve in Fig. 2(b), we also see that the standard deviation of the bond length distribution (indicated by the error bars) increases prior to each plastic shear deformation. Theoretical and numerical analysis shows that this phenomenon can be attributed to the Poisson effect. Qualitatively, as the crystalline sheet is stretched along one direction ( $u_{xx} > 0$ ), it shrinks in the perpendicular direction ( $u_{zz} < 0$ ), enlarging the dispersion in the distribution of the bond length. This effect is illustrated in the inset of the upper panel in Fig. 2(b), where the left and right triangles represent an elementary cell in the triangular lattice before and after the deformation.

Here, we present a quantitative geometric analysis based on the inset in Fig. 2(b) to explain the observed variation of the error bars on the  $\langle \ell \rangle$ - $\Gamma$  curve. In the deformed triangle,  $\ell_2 = \sqrt{(\ell_1/2)^2 + d_1^2}$ , where  $\ell_1 = (1 + \Gamma)\ell_0$ . By the definition of Poisson's ratio  $\sigma = -u_{zz}/u_{xx}$ , we have  $d_1 = (1 - \sigma\Gamma)d_0$ , where  $\sigma$  is the Poisson's ratio. We finally obtain an upper bound estimation for the

dispersion of the bond length distribution:

$$\begin{aligned} \frac{\delta \ell}{\ell_0} &= \frac{\ell_1 - \ell_2}{\ell_0} \\ &= 1 + \Gamma - \sqrt{1 + \frac{1 - 3\sigma}{2}\Gamma + \frac{1 + 3\sigma^2}{4}\Gamma^2} \\ &= \frac{3}{4}(1 + \sigma)\Gamma - \frac{3}{32}(1 + \sigma)^2\Gamma^2 + O(\Gamma^4). \end{aligned} \quad (11)$$

For  $\sigma = 1/3$ ,  $\delta \ell/\ell_0 = \Gamma - \Gamma^2/6 + O(\Gamma^4)$ , where the coefficient in the quadratic term is much less than that in the linear term. As such, the dispersion of the bond length distribution increases approximately linearly with  $\Gamma$ . This is in agreement with the numerical results in Fig. 2(b), where the relative reduction of the slope of  $\delta \ell(\Gamma)$  is less than 5% in the range of  $\Gamma \in [0, \Gamma_1]$ . The preceding argument based on the deformation of the elementary triangle could be extended to the case of a tilted lattice in mechanical equilibrium for  $\Gamma > \Gamma_1$  in Fig. 2(b). The conclusion remains valid that the dispersion of the bond length distribution is enlarged with the expansion of the cylinder.

Now, we analyze the plastic shear deformation from the perspective of the displacement field, as shown in Fig. 2(c). The displacement field is constructed based on the two particle configurations in mechanical equilibrium on the cylinders of radii  $R$  and  $R + \delta R$  in an expansion. Specifically, we project each particle in the latter particle configuration radially (along the direction of  $-\hat{e}_r$ ) onto the cylinder of radius  $R$ . The difference of the projected particle configuration and the original one on the cylinder of radius  $R$  yields the displacement field. Fig. 2(c) shows that the displacement field in a shear event is featured with the vortex structure. The coherent displacements of the particles in the vortex region are driven by the anti-parallel displacement vectors along the two adjacent shear bands. The shear-driven emergence of vortices, which is widely seen in fluids, has been reported in a compressed 2D lattice system [25]. Here, we show that a stretched lattice also supports the vortex structure under shear deformation, indicating the generality of the scenario of shear-driven vortex structure in solid mechanical systems.

## 3. Glide of dislocations in intermediate states

In the mechanical relaxation process for the case presented in Fig. 2, dislocations are observed within the shear band in the intermediate states; the intermediate states refer to the particle configurations in the mechanical relaxation process of the system at a given value of the expansion factor  $\Gamma$ . The remaining region of the crystalline sheet is free of topological defects. The results are recorded in Fig. 2(c). A dislocation consists of a pair of five- and seven-fold disclinations, which are indicated by the red and green dots in Fig. 2(c). A  $p$ -fold disclination refers to a point whose coordination number is equal to



$p$ , and it represents a fundamental topological defect in the triangular lattice [46].

Figure 2(c) shows that on the early stage of the relaxation process, a pair of dislocations labeled 1 simultaneously emerge on the adjacent shear bands. The subsequent migration of the dislocations is indicated by the labels 2, 3 and 4. The values of the simulation steps at the labels from 1 to 4 are  $n_s = 27,000, 29,500, 30,500$ , and  $31,000$ , respectively. Here, the numerical experiment at a fine simulation step allows us to capture the anti-parallel glide motion of the pair of the dislocations along the shear bands, which facilitates the shear deformation.

To understand the anti-parallel glide motion of the dislocations, we examine the force on the pair of the dislocations. The presence of the dislocation causes the deformation of an originally perfect crystal. In the small panel in Fig. 2(c), we show the deformed crystal lattice near a dislocation (the pair of green and red dots) on the shear bands. By the lines along the crystal lattice, we show that the effect of the dislocation is to insert an extra array of particles. In the continuum elasticity description, the property of the dislocation is characterized by the contour integral of the resulting displacement field enclosing the dislocation concerned [38]. It leads to the Burgers vector  $\vec{b}$  whose magnitude is equal to the lattice spacing. The Burgers vector is a topological quantity in the sense that it is independent of the geometry of the contour.

The Burgers vector specifies the direction of the glide motion of the dislocation [53]. In the inset of Fig. 2(c), the Burgers vector  $\vec{b}$  associated with the dislocation on the left shear band is plotted on the  $x$ - $z$  plane.  $\vec{b}$  is perpendicular to the connecting line of the five- and seven-fold disclinations and it makes an angle  $\phi$  with respect to the  $x$  axis. The signs of the Burgers vectors associated with the pair of dislocations on the adjacent shear bands are opposite.

The dislocation that is characterized by the Burgers vector  $\vec{b}$  is subject to the Peach-Koehler force in the external stress field  $\sigma_{ij}^{(e)}$  [54]:

$$f_i = -\varepsilon_{ij} \sigma_{jk}^{(e)} b_k, \quad (12)$$

where  $\varepsilon_{ij}$  is the anti-symmetric tensor. The Burgers vector on the  $x$ - $z$  plane is subject to the stress field in Eq.(5). From Eq.(12), we obtain the  $z$  component of the Peach-Koehler force:  $f_z = E\Gamma b_x$ . The  $x$  component of the force is zero. Therefore, the component of the Peach-Koehler force along the direction of the Burgers vector is

$$\begin{aligned} f_{\vec{b}} &= f_z \cos\left(\frac{\pi}{2} - \phi\right) \\ &= \frac{1}{2} E\Gamma b \sin(2\phi), \end{aligned} \quad (13)$$

which reaches maximum at  $\phi = \pi/4$  or  $\phi = 5\pi/4$ . Eq.(13) shows that  $f_{\vec{b}}$  is invariant in the transformation of  $\phi \rightarrow \phi + \pi$ . It indicates that the Peach-Koehler forces along the Burgers vectors of opposite signs are anti-parallel. This explains the observed anti-parallel glide

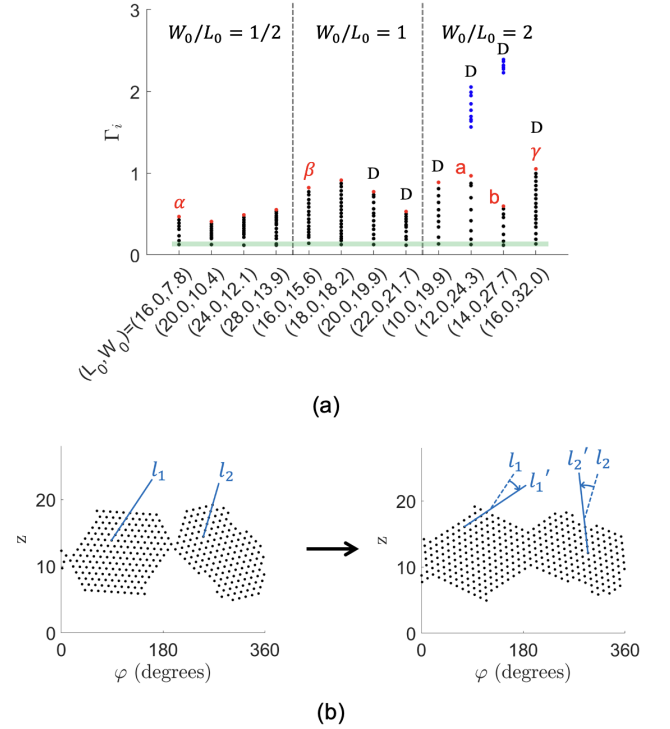


FIG. 3: Characterization of the intermittent plastic deformation process. (a) Plot of the critical values of  $\Gamma$  for the crystalline sheets of varying size and aspect ratio. The critical value of  $\Gamma$  is recorded for each plastic event in the expansion process. The complete fracture (disconnection) of the crystalline sheet wrapping the cylinder occurs at the terminal dots (in red). In the cases marked by letter D, topological defects remain in the mechanically relaxed lowest energy states. (b) The rotate-and-reconnect phenomenon after the complete fracture of the crystalline sheet. The value of  $\Gamma$  is increased from  $\Gamma = 1.547$  to  $\Gamma = 1.564$  in the two particle configurations. The post-fracture critical values of  $\Gamma$  are indicated by the blue dots in (a).

motion of the dislocations along the adjacent shear bands in Fig. 2(c).

Here, it is of interest to note that dislocations in cylindrical crystals exhibit rich phenomena despite of the zero Gaussian curvature of the cylindrical surface [42]. Besides the glide motion parallel to the Burgers vector, dislocations also climb perpendicular to the Burgers vector; the growth of the cell walls of rod-shaped bacteria may be regarded as mediated by dislocation climb [53]. Furthermore, in tubular crystal, which is modeled by the deformable network of harmonic springs in cylindrical topology, dislocation glide and its connection to the re-configuration of the lattice in terms of parastichy transition have been investigated by the combination of analytical continuum elasticity theory and numerical simulations [44]. In Ref. [44], the stress is applied along the axis of the tube, and the dislocation glide is realized by bond flip in the triangular lattices of spring bonds. The distinct physical mechanisms underlying the glide of dis-

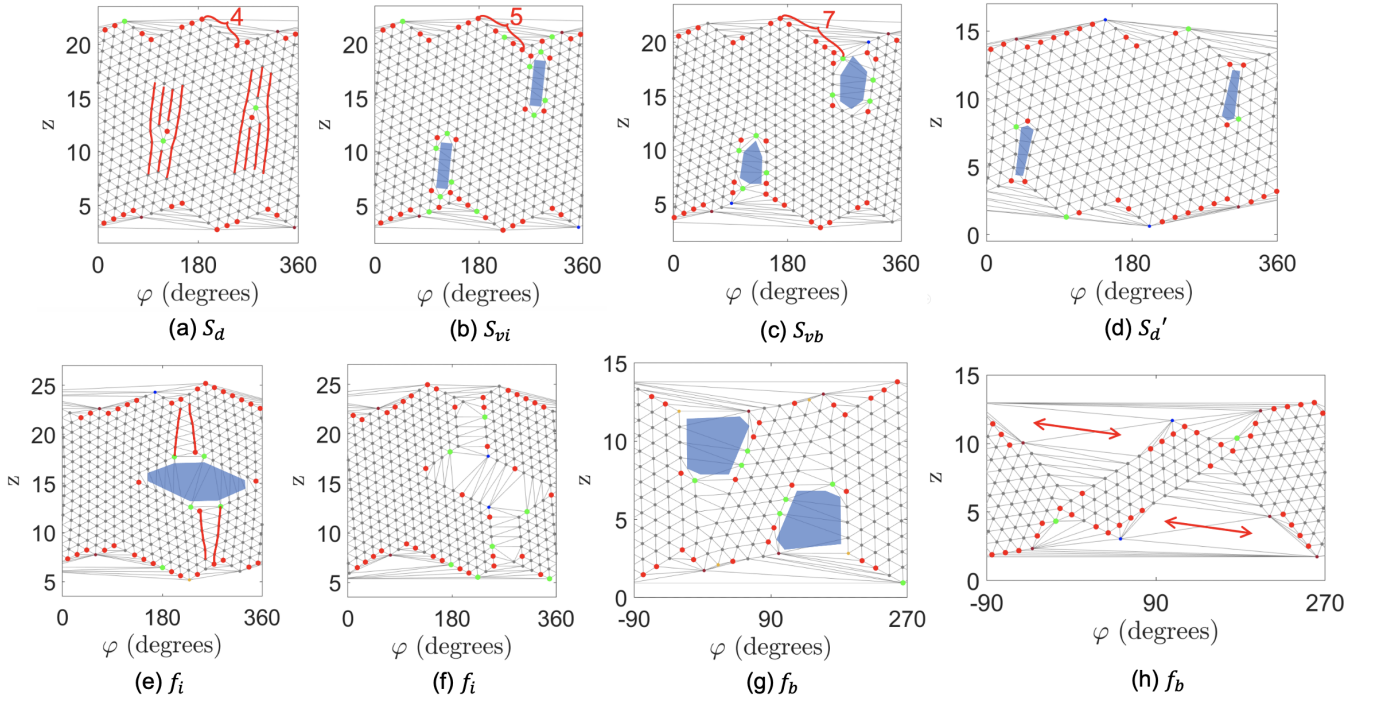


FIG. 4: Characteristic defect structures define the stable states in the fracture process of the crystalline sheet. (a)-(c) The fracture process in the example case of  $L_0 = 13.0$  and  $W_0 = 25.1$  follows the sequence of  $S_d \rightarrow S_{vi} \rightarrow S_{vb}$ , where the symbols refer to the defect states defined by the emergence of isolated dislocations (a), elongated vacancies in the interior of the lattice (b), and fractures at the boundary (c). (d) The defect state  $S_{d'}$  is characterized by the presence of isolated dislocations and the associated strips of square plaquettes (highlighted in blue) in the background of the triangular lattice. (e)-(f) and (g)-(h) show the fracture modes  $f_i$  and  $f_b$  under which the disconnection of the sheet is initiated from the interior and the boundary of the sheet, respectively.

locations in the lattices of spring bonds and L-J particles share a common topological consequence. Specifically, dislocation glide leads to the changes in the parastichy numbers in the former case and the stepwise transformations in the latter case; the reason is that the effect of a dislocation in a triangular lattice is to insert an array of particles [38].

#### 4. Characterization of the intermittency of plastic deformations

We systematically investigate the plastic deformations in the expansion of crystalline sheets of varying geometry. The value of  $\Gamma$  is recorded for each plastic event in the expansion process, including the formation of steps on the boundary of the sheet and the relocation of particles in the interior of the lattice. The results for crystalline sheets of typical aspect ratios are grouped and presented in Fig. 3(a). In Fig. 3(a), the series of the critical values of  $\Gamma$  as represented by the columns of dots indicate the intermittent nature of the plastic deformations of the stretched crystalline sheet under the gradual expansion of the cylinder. Note that in the cases marked by letter D in Fig. 3(a), topological defects remain in the mechanically relaxed lowest energy states. The defect-based fracture

processes will be discussed in Sec. III C.

From Fig. 3(a), we observe that the first critical values  $\Gamma_1$ , at which the originally crystalline lattice is subject to initial plastic deformation, are located within the thin bar in green and they are insensitive to the size and aspect ratio of the crystalline sheet. Statistical analysis of the data presented in Fig. 3(a) shows that for the crystalline sheets of varying size and aspect ratio,  $\Gamma_1$  takes a relatively uniform value:  $\Gamma_1 = 0.126 \pm 0.008$ . In contrast, the values of  $\Gamma_f$  as indicated by the red dots in Fig. 3(a), at which the crystalline sheet is completely fractured, exhibit appreciable discrepancy not only for the crystalline sheets of different aspect ratios but also for those of different sizes and identical aspect ratio.

Here, we compare the crystalline sheets  $\alpha$ ,  $\beta$  and  $\gamma$  of identical length  $L_0$  and varied width  $W_0$  in Fig. 3(a) and find that the value of  $\Gamma_f$  is larger for a wider sheet. It suggests that increasing the width of the crystalline sheet enhances its ability to resist fracture upon the expansion. It is noticed that in general the dots in the columns are unevenly distributed, implying the sensitivity of the critical values of  $\Gamma$  to the stretching deformation for the highly stretched crystalline sheet. The enhanced sensitivity of the crystalline sheet under stronger stretching is confirmed by checking the example case of  $(L_0, W_0) = (16.0, 15.7)$  at varying step size. Specifically,



as the value of the step size is varied in the range from  $s = 5 \times 10^{-4}$  to  $s = 10^{-3}$ , the critical value of  $\Gamma_1$  is varied in the narrow range of  $\Gamma_1 = 0.129 \pm 0.008$ . In contrast, the critical value of  $\Gamma_f$  is subject to a larger fluctuation of  $\Gamma_f = 0.749 \pm 0.228$ , which could be attributed to the enhanced sensitivity of the highly stretched crystalline sheet prior to complete fracture. Note that the intermittent nature of the plastic shear deformations is unchanged with the variation of the step size.

The numerical approach also captures post-fracture events. Specifically, in the case of  $(L_0, W_0) = (12.0, 24.3)$  [labeled by *a* in Fig. 3(a)], the two crystal patches connected by a neck whose width is as thin as one lattice spacing (which is regarded as being disconnected by our practical criterion) are observed to rotate and reconnect neatly, as shown in Fig. 3(b); the value of  $\Gamma$  is increased by 1.1% (from  $\Gamma = 1.547$  to  $\Gamma = 1.564$ ). In this process, the rotational motion of the crystal patches along the opposite directions, which can be excited without costing much energy, is the key to triggering the energetically favored reconnection event. Similar process is observed in the case of  $(L_0, W_0) = (14.0, 27.7)$  [labeled by *b* in Fig. 3(a)]. It seems that the crystalline sheet exhibits a strong tendency to reconnect even if the disconnection has already occurred, all out of the attractive nature of the L-J potential in the stretched regime. Further stretching the stable particle configuration in the reconnected state in Fig. 3(b) leads to a series of plastic deformations; the corresponding critical values of  $\Gamma$  are recorded in Fig. 3(a) by the blue dots.

### C. Defect-based fracture mechanism

Systematic investigations of crystalline sheets of varying geometry shows that topological defects may remain in the mechanically relaxed lowest energy states. We shall show that these topological defects provide a fracture mechanism that is distinct from the defect-free fracture process as discussed in the previous subsection. In the latter process, dislocations vanish via the continuous slide along the shear band.

We first examine the fracture process in a specific example case of  $L_0 = 13.0$  and  $W_0 = 25.1$ . The typical lattice configurations in mechanical equilibrium are presented in Figs. 4(a)-4(c). The red and green dots represent five- and seven-fold disclinations. With the expansion of the cylinder, we first observe the emergence of isolated dislocations (5–7 disclination pairs) in the interior of the lattice and the simultaneous formation of step structures on the boundaries of the lattice. In Fig. 4(a), by the lines along the crystal lattice, we show that the opposite signs of the Burgers vectors associated with the two dislocations correspond to the insertion of particle arrays along opposite directions.

Increasing the value of  $\Gamma$  from  $\Gamma = 0.44$  [Fig. 4(a)] to  $\Gamma = 0.48$  [Fig. 4(b)] leads to the instability of the isolated dislocations, resulting in the stretch-driven formation of

elongated vacancies (interior fractures) as highlighted in blue in Fig. 4(b). This scenario is fundamentally different from the glide of the dislocations in the crystalline sheet of smaller width in Fig. 2. Here, the dislocations are anchored in space and they serve as the seeds for the subsequent vacancy structures. Under the gradual expansion of the cylinder, these interior fractures are further torn apart and extended to the boundaries of the lattice as shown in Fig. 4(c). The characteristic defect states in Figs. 4(a)-4(c) are denoted as  $S_d$  (isolated dislocations),  $S_{vi}$  (elongated vacancies in the interior of the lattice) and  $S_{vb}$  (elongated vacancies at the boundary), respectively. In the expansion of the cylinder, we also notice the growth of the step structure in its height; the step heights are indicated by the numbers.

The extension of the elongated vacancies in the defects states  $S_{vi}$  and  $S_{vb}$  under the uniaxial stretching of the crystalline sheet could be understood in the framework of the Griffith theory for crack stability [55]. According to the Griffith theory, the propagation of an existing crack in a crystal occurs when the decrease in the elastic strain energy exceeds the increase in surface energy created by the new crack surface. The scenario of the crack propagation based on the continuum Griffith theory has been developed in a series of atomic-scale simulations by incorporating the discrete lattice structure of the crystal [56], the role of dislocations [57], the strain-dependence of the Young's modulus and surface energy as well as the effect of lattice trapping [58]. In our system, the observed extension of the elongated vacancies at zero temperature is also driven by the reduction of energy according to the steepest descent algorithm. It is of interest to carry out detailed analysis of different energy contributions in the crack process; it is beyond the scope of current investigation.

The fracture process of the crystalline sheet shown in Figs. 4(a)-4(c) could be represented by the sequence of  $S_d \rightarrow S_{vi} \rightarrow S_{vb}$ . This route of fracture is distinct from defect-free fracture process in Fig. 2, where topological defect emerge only in the intermediate states. Here, the emergence of defects implies that the fracture mechanism based on pure shear deformation like in the case of Fig. 2 becomes insufficient for the crystalline sheet to withstand the expansion of the cylinder. A new fracture mechanism based on the proliferation of defects is activated in a highly stretched crystalline sheet to adapt to the expanding cylinder. Here, we also report the observation of the strips of square plaquettes [highlighted in blue in Fig. 4(d)] embedded in the triangular lattice in the partial shear of the lattice; the particle configuration is in mechanical equilibrium.

Upon the gradual expansion, the highly stretched crystalline sheet is ultimately completely fractured. We examine the entire fracture processes of crystalline sheets of varying geometry and find that the disconnection of the sheet follows three kinds of modes. In the first mode, the crystalline sheet is completely fractured via the continuous slide of the lattice along the shear band as shown

$L_0 \backslash W_0$	10.0	15.0	20.0	25.0	30.0
10.4	$S_0 \rightarrow S_{vi} \rightarrow S_0 \rightarrow f_s$	$S_0 \rightarrow f_s$	$S_0 \rightarrow f_s$	$S_0 \rightarrow f_s$	$S_0 \rightarrow f_s$
14.7	$S_0 \rightarrow S_d \rightarrow S'_d \rightarrow S_{vi} \rightarrow S_{vb} \rightarrow f_b$	$S_0 \rightarrow f_s$	$S_0 \rightarrow f_s$	$S_0 \rightarrow f_s$	$S_0 \rightarrow f_s$
19.9	$S_0 \rightarrow S_{vi} \rightarrow f_s \& f_i$	$S_0 \rightarrow S_d \rightarrow S_0 \rightarrow S_d \rightarrow S_0 \rightarrow S_{vb} \rightarrow f_s \& f_b$	$S_0 \rightarrow S_{vi} \rightarrow S_0 \rightarrow S_{vi} \rightarrow S_{vi} \& S_{vb} \rightarrow f_s \& f_i \& f_b$	$S_0 \rightarrow f_s$	$S_0 \rightarrow f_s$
25.1	$S_0 \rightarrow S_{vb} \rightarrow f_s \& f_b$	$S_0 \rightarrow S_d \rightarrow S_0 \rightarrow S_d \rightarrow S_0 \rightarrow S_d \rightarrow S_{vi} \rightarrow S_{vb} \rightarrow f_s \& f_b$	$S_0 \rightarrow S_d \rightarrow S_0 \rightarrow S'_d \rightarrow S_{vb} \rightarrow f_s \& f_b$	$S_0 \rightarrow f_s$	$S_0 \rightarrow f_s$
30.3	$S_0 \rightarrow S_{vi} \rightarrow f_i \& f_s$	$S_0 \rightarrow S_d \rightarrow S_0 \rightarrow S_d \rightarrow S'_d \rightarrow S_{vi} \rightarrow S_{vb} \rightarrow f_b \& f_s$	$S_0 \rightarrow S_{vi} \rightarrow f_s \& f_i$	$S_0 \rightarrow S_{vi} \rightarrow S_0 \rightarrow S_{vb} \rightarrow f_s \& f_b$	$S_0 \rightarrow S_q \rightarrow S_q \& S_{vb} \rightarrow S_q \& S_{vb} \& S_{vi} \rightarrow S_{vb} \& S_{vi} \rightarrow S_{vb} \& S_q \rightarrow S_{vb} \rightarrow S_0 \rightarrow S_q \rightarrow S_{vi} \rightarrow S_0 \rightarrow S_d \rightarrow S_0 \rightarrow S_{vb} \rightarrow f_s \& f_b$

TABLE I: The phase diagram for the defect-free and defect-based fracture mechanisms, as distinguished by the blue and black font colors, respectively. The sequences show the stable states in the fracture process. The symbols  $S_*$  refer to the defect states defined by the emergence of isolated dislocations ( $S_d$  and  $S'_d$ ), quadrupoles ( $S_q$ ) and elongated vacancies in the interior ( $S_{vi}$ ) and on the boundary ( $S_{vb}$ ) of the lattice. The defect-free state is indicated by  $S_0$ . The disconnection behaviors of the crystalline sheet are characterized by the three kinds of modes:  $f_i$  (via the interior fractures),  $f_b$  (via the fractures on the boundary) and  $f_s$  (via defect-free plastic shear deformation).

in Fig. 2. This mode is denoted as  $f_s$ . In the second and third modes, the disconnection of the sheet is initiated from the interior and the boundary of the lattice, respectively. They are denoted as  $f_i$  and  $f_b$ , respectively.

Specifically, the  $f_i$  mode is illustrated in Figs.4(e) and 4(f). Under the longitudinal stretching, the eye-shaped hole (highlighted in blue) is fractured approximately at the locations of  $\phi = \pi/2$  and  $\phi = 3\pi/2$  (marked by the red lines), where  $\phi$  is the polar angle. These preferred fracture sites could be understood by the model of the circular hole under the uniform horizontal tension  $S$ . According to the continuum elasticity theory, the azimuthal component of the stress tensor  $\sigma_{\phi\phi}$  around the circular hole in an isotropic elastic medium reaches maximum  $(\sigma_{\phi\phi})_{\max} = 3S$  at  $\phi = \pi/2$  or  $\phi = 3\pi/2$  [38, 59]. In Fig.4(e), the vertical fractures are driven by the stress  $\sigma_{\phi\phi}$  and they tend to occur on sites where  $\sigma_{\phi\phi}$  reaches maximum. In other words, the fractures initiated from the interior of the lattice could be attributed to the stress-focusing effect around the preexistent vacancies.

In the  $f_b$  mode as shown in Figs.4(g) and 4(h), the disconnection of the crystalline sheet is caused by the extension of the pre-existent fractures on the boundary (highlighted in blue). Here, we shall point out that in some cases, the disconnection process involves the combination of the three kinds of modes ( $f_s$ ,  $f_i$ , and  $f_b$ ). For example, we observe the realization of the complete fracture via the simultaneous slide along the shear band and the extension of the fracture on the boundary. This disconnection mode is denoted as  $f_s \& f_b$ .

In Table I, we list all of the stable states in the fracture process of the stretched crystalline sheets of typical geometries upon the gradual expansion of the cylinder.

$S_0$  refers to the defect-free state. The other symbols  $S_*$  refer to the defect states defined by the emergence of isolated dislocations ( $S_d$  and  $S'_d$ ), quadrupoles ( $S_q$ ) and elongated vacancies in the interior ( $S_{vi}$ ) and on the boundary ( $S_{vb}$ ) of the lattice. The disconnection behaviors of the crystalline sheet are summarized by the three kinds of modes:  $f_i$ ,  $f_b$  and  $f_s$ .

From the columns of the entries in Table I, we see that increasing the width of the crystalline sheet leads to the transition in the fracture mechanism from the defect-free to the defect-based plastic deformations, which are distinguished by the blue and black colors in the Table. The transition in the fracture mechanism with the increase of  $W_0$  suggests that the coordinated movement of the particle array along the shear band in the defect-free fracture process is ultimately disrupted along a sufficiently long shear band. From the perspective of topological defects, the excited dislocations induce the formation of elongated vacancies prior to gliding to the boundary along a long shear band. Note that in Fig. 3 all of the cases in the group of  $W_0/L_0 = 2$  and some cases in the group of  $W_0/L_0 = 1$  (indicated by letter D) belong to the category of defect-based fracture and the remaining cases (with  $W_0/L_0$  being equal to one or less) follow the defect-free fracture mode, which is consistent with the results presented in Table I. Here, we shall point out that even in the defect-free fracture mechanism as shown in Fig. 2, dislocations arise in the intermediate states to facilitate the plastic shear deformation via the glide motion; these defects ultimately vanish in the mechanically relaxed states in crystalline sheets of short width. From Table I, we also notice that the crystalline sheet tends to be disconnected from the interior (in the  $f_i$  mode) with the appearance

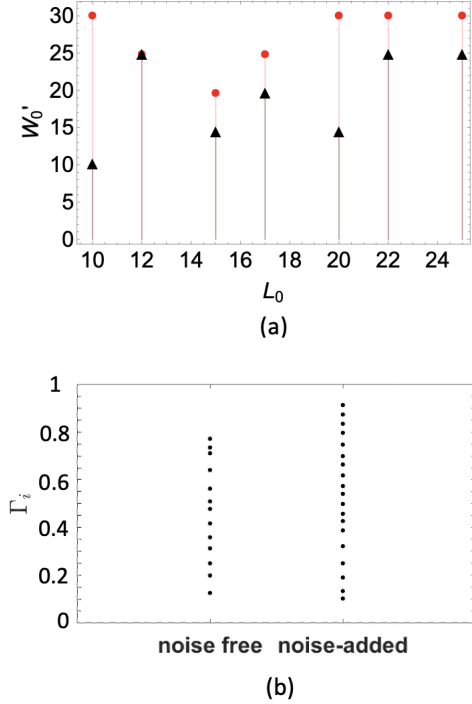


FIG. 5: Effect of noise on the fracture of the crystalline sheet. (a) Plot of  $W'_0$  versus the length of the crystalline sheet  $L_0$  in the presence and absence of noise, as indicated by dots (red) and triangles (black), respectively. For  $W \leq W'_0$ , the interior of the crystalline sheet is overall free of defects in the fracture process (except a few transient defect events). (b) Comparison of the critical values  $\Gamma_i$  in the intermittent plastic shear deformations in the presence and absence of noise.  $L_0 = 20.0$  and  $W_0 = 19.9$ .

of interior vacancies (in the defect state  $S_{vi}$ ); otherwise, the disconnection occurs from the boundary of the sheet (in the  $f_b$  mode).

#### D. Effects of noise and initial lattice orientation

In this subsection, we discuss the effects of noise and initial lattice orientation on the plastic deformation of the stretched crystalline sheet.

The stable states in the phase diagram in Table I are obtained by mechanical relaxations at zero temperature. We further investigate the effect of noise on the fracture behavior of the crystalline lattice. To add noise in the mechanical relaxation process, we introduce an uncertainty in the update of the particle positions in simulations. Specifically, the new position of particle  $i$  that is originally at position  $\vec{r}_i$  is located at  $\vec{r}_i'' = \vec{r}_i' + c_0 \vec{\xi}$ .  $\vec{r}_i' = \vec{r}_i + \hat{F}_i s$  is the new position of particle  $i$  under the mechanical relaxation algorithm at zero temperature, where  $\hat{F}_i$  is the normalized force on particle  $i$ . The second term  $c_0 \vec{\xi}$  represents a random displacement of maximum magnitude  $c_0$ .  $c_0 = 0.1s$ , where  $s$  is the step size.

$\vec{\xi}$  is a random 2D vector whose orientation and magnitude are uniformly distributed in the ranges of  $[0, 2\pi)$  and  $[0, 1]$ , respectively. With the introduction of the noise in the relaxation process, we still observe the intermittent plastic shear deformations and the transition from the defect-free to the defect-based plastic deformation as the width  $W_0$  of the crystalline lattice of given length  $L_0$  is increased.

Simulations show that adding the noise at the level of  $c_0 = 0.1s$  tends to facilitate the glide motion of the dislocations and thus increase the critical value of  $W_0$  above which the defect-free to defect-based transition occurs. In Fig. 5(a), we present the plot of  $W'_0$  versus the length of the crystalline sheet  $L_0$  in the presence and absence of noise, as indicated by dots (red) and triangles (black), respectively. For  $W \leq W'_0$ , the interior of the crystalline sheet is overall free of defects in the fracture process except a few transient defect events. These transient defect events in the interior of the crystalline sheet do not affect the fracture process in the sense that no stress-focusing effect around the defect is observed. For example, in the system of  $L_0 = 12$  and  $W_0 = 19.9$  in the absence of noise, a topologically neutral compound defect (consisting of one nine-fold disclination surrounded by three five-fold disclinations) appears at  $\Gamma_{19} = 0.14$ , transforms into a vacancy (a pair of dislocations) at  $\Gamma_{21} = 0.16$ , and disappears at  $\Gamma_{29} = 0.22$ . In the system of  $L_0 = 22$  and  $W_0 = 10.4$ , we observe the appearance of a pair of isolated dislocations at  $\Gamma_{35} = 0.28$ , which disappears upon a gentle further expansion at  $\Gamma_{37} = 0.29$ . From Fig. 5(a), we see that the value of  $W'_0$  is overall increased with the introduction of the noise (red dots). Here, we shall report an exceptional case in the presence of noise at  $L_0 = 15$ . For  $W \leq 19.9$ , the fracture process is defect-free. While the defect-free to defect-based transition occurs at  $W_0 = 25.1$ , the fracture process becomes defect-free again at  $W_0 = 30.3$ . This case implies the complication brought by the noise.

We also examine the effect of noise on the critical values  $\Gamma_i$  in the intermittent plastic shear deformations. A typical case is presented in Fig. 5(b) for  $L_0 = 20.0$  and  $W_0 = 19.9$ . Comparison of the critical values  $\Gamma_i$  in the presence and absence of noise shows that the first critical value  $\Gamma_1$  is subject to a much smaller variation in comparison with that of the critical value  $\Gamma_f$ , at which the crystalline lattice is completely fractured. The enhanced sensitivity of the highly stretched crystalline sheet implies the appearance of many nearly-equivalent paths over the energy landscape in the highly-stretched regime. This observation is consistent with the variation of the critical values  $\Gamma_i$  by increasing the step size, which effectively introduces noise in the relaxation process.

In preceding discussions, we focus on the plastic deformations of crystalline lattices at the tilt angle of 60 degrees, i.e., the angle of the inclined principal axis of the lattice with respect to the  $x$  axis is 60 degrees, as shown in Fig.1(a). In general, a seamless triangular lattice wrapping the cylinder can be generated by a peri-

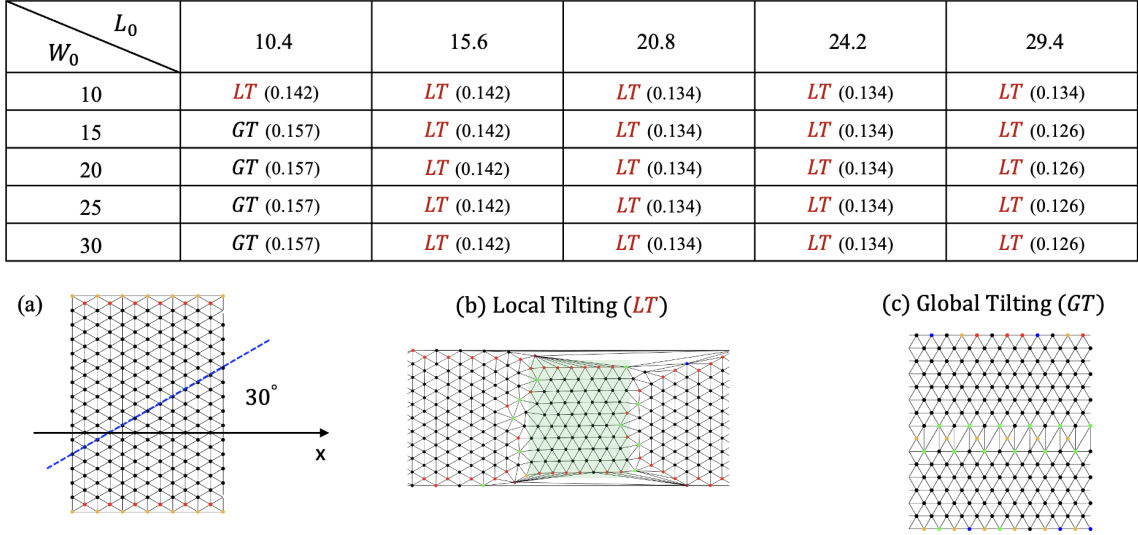


FIG. 6: The abrupt tilting transition of the crystalline lattices initially at the tilt angle of 30 degrees. The table shows the two distinct modes of tilting transition in crystalline sheets of varying geometry; the critical values of  $\Gamma$  at which the tilting transition occurs are listed besides. (a) The undeformed crystalline lattice at the tilt angle of 30 degrees. (b) In the local tilting (denoted as *LT*), the crystalline lattice is partly tilted to the 60 degrees configuration; the tilted domain is highlighted in green. (c) In the global tilting (denoted as *GT*) as shown in (c), the entire lattice is tilted from the original 30 degrees configuration to the 60 degrees configuration. The subsequent fracture of the lattice upon further expansion is characterized by a series of intermittent plastic shear deformations, and it is similar to the case of the crystalline sheet whose tilt angle is 60 degrees.

odicity vector, which is characterized by the phyllotactic index  $[\ell, m, n]$ , where  $m \geq n$  and  $\ell = m + n$  [39, 43]. The lattice at the tilt angle of 60 degrees is represented by  $[h, h, 0]$ , where  $hr_0$  is the perimeter of the cylinder and  $r_0$  is the lattice spacing. Here, we consider another typical case that the crystalline lattice wraps the cylindrical surface at the tilt angle of 30 degrees [39, 43]; see Fig. 6(a). The corresponding phyllotactic index is  $[p, p/2, p/2]$ , where  $pr_0$  is length of the spiral (i.e., the inclined principal axis at the tilted angle of 30 degrees wrapping the cylinder) within a pitch.

Upon the gradual expansion of the cylinder at the same rate as in the case of the tilt angle of 60 degrees, it is found that the crystalline sheet exhibits an abrupt transition from the 30 degrees configuration to the 60 degrees configuration, either locally or globally depending on the geometry of the crystalline sheet. The transition occurs abruptly under a gentle expansion of the cylinder by 0.7%. The results are summarized in the table in Fig. 6. In the local tilting (denoted as *LT*), the crystalline lattice is partly tilted to the 60 degrees configuration as shown in Fig. 6(b). The tilted domain is highlighted in green. Grain boundaries are formed at the interface of the domains of distinct tilt angles. In the global tilting (denoted as *GT*) as shown in Fig. 6(c), the entire lattice is tilted from the original 30 degrees configuration to the 60 degrees configuration except the thin horizontal belt; in some cases, the belt vanishes upon a further gentle expansion of the cylinder. With the further expansion of the cylinder, the subsequent fracture of the lattice is characterized by a series of intermittent plastic shear de-

formations, and it is similar to the case of the crystalline sheet whose tilt angle is 60 degrees. The critical values of  $\Gamma$  at which the abrupt tilting transition occurs are recorded in the table in Fig. 6.

#### IV. CONCLUSION

In summary, we study the adaptations of crystalline sheets to uniaxial stretching deformation and reveal the intermittent plastic shear deformations leading to the complete fracture (disconnection) of the crystalline sheet wrapping the cylinder. Systematic investigations of crystalline sheets of varying geometry show that the fracture processes can be classified into the defect-free and defective categories depending on the emergence of topological defects. The computational approach reveals the characteristic mechanical and geometric patterns arising in the crystalline sheet system in response to the stretching deformation, including the shear-driven intermittent lattice tilting, the vortex structure in the displacement field, and the emergence of mobile and anchored dislocations as plastic excitations. Uniaxial stretching represents a fundamental mechanical agitation and it also occurs in locally stretched packings of particles in the contexts like crystal growth and 2D assembly. As such, the results presented in this work may yield insights into the subtle role of stretching deformation in triggering structural instabilities of 2D regular packings of particles in general.

## V. ACKNOWLEDGEMENTS

This work was supported by the National Natural Science Foundation of China (Grants No. BC4190050).

- 
- [1] E. Cerda and L. Mahadevan, Phys. Rev. Lett. **90**, 074302 (2003).
  - [2] M. Marder, R. D. Deegan, and E. Sharon, Physics Today **60**, 33 (2007).
  - [3] B. Audoly and Y. Pomeau, *Elasticity and Geometry* (Oxford University Press, Oxford, 2010).
  - [4] J. Chopin, V. Démery, and B. Davidovitch, J. Elast. **119**, 137 (2015).
  - [5] T. Yu and L. Zhang, Int. J. Mech. Sci. **28**, 729 (1986).
  - [6] J.-C. G  minard, R. Bernal, and F. Melo, Eur. Phys. J. E **15**, 117 (2004).
  - [7] A. K. Harris, P. Wild, and D. Stopak, Science **208**, 177 (1980).
  - [8] E. Cerda, K. Ravi-Chandar, and L. Mahadevan, Nature **419**, 579 (2002).
  - [9] S. P. Lacour, S. Wagner, Z. Huang, and Z. Suo, Appl. Phys. Lett. **82**, 2404 (2003).
  - [10] T. Wang, Y. Yang, and F. Xu, Proc. R. Soc. London, Ser. A **478**, 20220149 (2022).
  - [11] E. Sharon, B. Roman, and H. L. Swinney, Phys. Rev. E **75**, 046211 (2007).
  - [12] B. Li, Y.-P. Cao, X.-Q. Feng, and H. Gao, Soft Matter **8**, 5728 (2012).
  - [13] N. Friedl, F. G. Rammerstorfer, and F. D. Fischer, Comput. Struct. **78**, 185 (2000).
  - [14] Y. Lecieux and R. Bouzidi, Adv. Eng. Softw. **50**, 57 (2012).
  - [15] C. Wang, L. Lan, and H. Tan, Phys. Chem. Chem. Phys. **15**, 2764 (2013).
  - [16] E. Puntel, L. Deseri, and E. Fried, J. Elast. **105**, 137 (2011).
  - [17] G. M. Grason and B. Davidovitch, Proc. Natl. Acad. Sci. U.S.A. **110**, 12893 (2013).
  - [18] J. Chopin and A. Kudrolli, Soft Matter **12**, 4457 (2016).
  - [19] T. Jules, F. Lechenault, and M. Adda-Bedia, Phys. Rev. E **102**, 033005 (2020).
  - [20] M.-C. Miguel, A. Mughal, and S. Zapperi, Phys. Rev. Lett. **106**, 245501 (2011).
  - [21] C. Negri, A. L. Sellerio, S. Zapperi, and M.-C. Miguel, Proc. Natl. Acad. Sci. **112**, 14545 (2015).
  - [22] N. P. Mitchell, V. Koning, V. Vitelli, and W. Irvine, Nat. Mater. **16**, 89 (2017).
  - [23] M. Liu, S. Yu, L. He, and Y. Ni, Soft Matter **18**, 5906 (2022).
  - [24] J. Chen and Z. Yao, Soft Matter **18**, 5323 (2022).
  - [25] H. Sun and Z. Yao, Phys. Rev. E **109**, 044802 (2024).
  - [26] P. Politi, G. Grenet, A. Marty, A. Ponchet, and J. Villain, Phys. Rep. **324**, 271 (2000).
  - [27] G. Meng, J. Paulose, D. R. Nelson, and V. N. Manoharan, Science **343**, 634 (2014).
  - [28] C. K  hler, R. Backofen, and A. Voigt, Europhys. Lett. **111**, 48006 (2015).
  - [29] L. Ma, X. Liu, A.-k. Soh, L. He, C. Wu, and Y. Ni, Soft Matter **15**, 4391 (2019).
  - [30] A. Dinsmore, M. F. Hsu, M. Nikolaides, M. Marquez, A. Bausch, and D. Weitz, Science **298**, 1006 (2002).
  - [31] J. Palacci, S. Sacanna, A. P. Steinberg, D. J. Pine, and P. M. Chaikin, Science **339**, 936 (2013).
  - [32] M. Bowick and P. Chaikin, Nat. Mater. **15**, 1151 (2016).
  - [33] D. L. Caspar and A. Klug, in *Cold Spring Harbor Symposia on Quantitative Biology* (Cold Spring Harbor Laboratory Press, 1962), vol. 27, pp. 1–24.
  - [34] J. Lidmar, L. Mirny, and D. R. Nelson, Phys. Rev. E **68**, 051910 (2003).
  - [35] W. Roos, R. Bruinsma, and G. Wuite, Nat. Phys. **6**, 733 (2010).
  - [36] J. E. Jones, Proc. R. Soc. London, Ser. A. **106**, 463 (1924).
  - [37] J. N. Israelachvili, *Intermolecular and Surface Forces* (Academic Press, New York, 2011), 3rd ed.
  - [38] L. D. Landau and E. M. Lifshitz, Theory of Elasticity, 3rd ed. (Butterworth-Heinemann, Oxford, UK, 1986).
  - [39] A. Mughal, H. Chan, D. Weaire, and S. Hutzler, Phys. Rev. E **85**, 051305 (2012).
  - [40] A. Amir and D. R. Nelson, Proc. Natl. Acad. Sci. U.S.A. **109**, 9833 (2012).
  - [41] D. R. Nelson, Annu. Rev. Biophys. **41**, 371 (2012).
  - [42] A. Amir, J. Paulose, and D. R. Nelson, Phys. Rev. E **87**, 042314 (2013).
  - [43] A. Mughal and D. Weaire, Phys. Rev. E **89**, 042307 (2014).
  - [44] D. A. Beller and D. R. Nelson, Phys. Rev. E **94**, 033004 (2016).
  - [45] J. A. Snyman and D. N. Wilke, *Practical Mathematical Optimization* (Springer, New York, 2005).
  - [46] D. R. Nelson, *Defects and Geometry in Condensed Matter Physics* (Cambridge University Press, Cambridge, 2002).
  - [47] D. Struik, *Lectures on Classical Differential Geometry* (Dover Publications, New York, 1988), 2nd ed.
  - [48] H. S. Seung and D. R. Nelson, Phys. Rev. A **38**, 1005 (1988).
  - [49] I. Berinskii and H. Altenbach, Acta Mech. **228**, 683 (2017).
  - [50] R. Asaro and W. Tiller, Metall. Mater. Trans. B. **3**, 1789 (1972).
  - [51] M. Grinfeld, in Dok. Akad. Nauk SSSR **290**, 1358 (1986) [Sov. Phys. Dokl. **31**, 831 (1986)].
  - [52] D. J. Srolovitz, Acta Metall. **37**, 621 (1989).
  - [53] J. P. Hirth and J. Lothe, *Theory of Dislocations* (John Wiley & Sons, 1982).
  - [54] M. Peach and J. Koehler, Phys. Rev. **80**, 436 (1950).
  - [55] A. A. Griffith, Philos. Trans. R. Soc. London A **221**, 163 (1921).
  - [56] M. Ippolito, A. Mattoni, L. Colombo, and N. Pugno, Phys. Rev. B **73**, 104111 (2006).
  - [57] K. S. Cheung and S. Yip, Phys. Rev. Lett. **65**, 2804 (1990).
  - [58] A. Mattoni, L. Colombo, and F. Cleri, Phys. Rev. Lett. **95**, 115501 (2005).
  - [59] S. Timoshenko and J. Goodier, *Theory of Elasticity*

(McGraw-Hill Book Company, 1951).